

Tensile properties of multi-material interfaces in 3D printed parts

Journal Article**Author(s):**

Lumpe, Thomas S.; Mueller, Jochen; Shea, Kristina

Publication date:

2019-01-15

Permanent link:

<https://doi.org/10.3929/ethz-b-000304518>

Rights / license:

[Creative Commons Attribution-NonCommercial-NoDerivatives 4.0 International](#)

Originally published in:

Materials & Design 162, <https://doi.org/10.1016/j.matdes.2018.11.024>



Tensile properties of multi-material interfaces in 3D printed parts

Thomas S. Lumpe*, Jochen Mueller, Kristina Shea

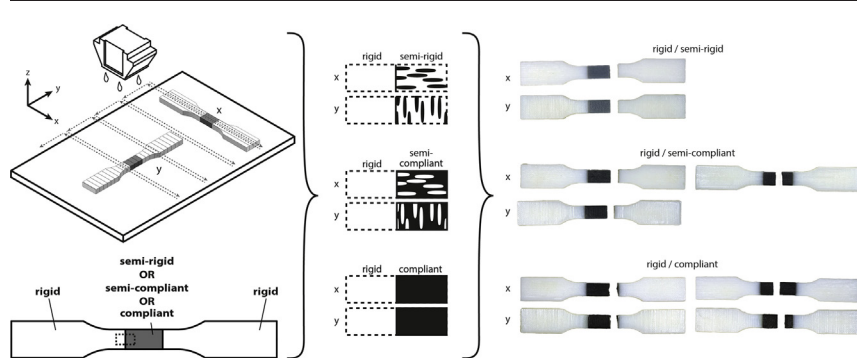
Engineering Design and Computing Laboratory, Department of Mechanical and Process Engineering, ETH Zurich, Tannenstrasse 3, 8092 Zurich, Switzerland



HIGHLIGHTS

- Interface strength of multi-material 3D printed parts depends not only on print parameters but also on material combination.
- Orientation of material interfaces with respect to the print head movement also strongly influences the interface strength.
- Some combinations of materials and interface orientations can reduce interface strength by 50% as well as increase it by 20%.

GRAPHICAL ABSTRACT



ARTICLE INFO

Article history:

Received 17 August 2018
 Received in revised form 8 November 2018
 Accepted 9 November 2018
 Available online 10 November 2018

Keywords:

Multi-material additive manufacturing
 Material interfaces
 Functionally graded materials
 Material jetting
 Material testing

ABSTRACT

Due to continuing progress in multi-material additive manufacturing, the design space for multifunctional and functionally graded materials and structures is significantly increased. To take full advantage of this capability, a solid understanding of the interface properties is critical, as it can significantly affect the overall mechanical behavior. This paper investigates the tensile strength of multi-material interfaces fabricated via material jetting. Tensile test specimens comprising two different materials, ranging from a rigid-brittle material to a compliant-rubbery one, are experimentally tested at room temperature. Strong dependencies on the material combination and the print orientation, i.e. the orientation of the specimens with respect to the movement of the print head, are found. Interfaces between rigid and compliant materials are mostly found to be as strong as the compliant material itself, whereas interfaces between two rigid materials show strength values reduced by up to 50% for particular print orientations. The findings enable designers to design more reliable multi-material structures while avoiding adverse material combinations and part orientations.

© 2018 Elsevier Ltd. This is an open access article under the CC BY-NC-ND license (<http://creativecommons.org/licenses/by-nc-nd/4.0/>).

1. Introduction

Multi-material 3D printing significantly extends the capabilities of conventional single-material 3D printing by allowing for simultaneous printing of different materials with mechanical properties ranging over several orders of magnitude [1]. One of the first and still most powerful technologies in the field is material jetting, often referred to as inkjet 3D printing. This process is characterized by the ability to eject

drops of material on demand [2], allowing for high resolution and hence geometric accuracy. This capability has been used in various fields to fabricate more advanced products, for example in biomedical engineering [3,4], electronics [5,6], and for wearable devices [7]. The large variety of available materials [8–10] is further expanded by the possibility to mix different compatible base materials during printing to obtain materials with intermediate properties [11].

From a design perspective, the ability to print parts from multiple materials increases the already vast design space of additive manufacturing (AM) further. The complex (micro-)mechanical behaviors of the different materials and interfaces have to be considered to

* Corresponding author.
 E-mail address: tlumpe@ethz.ch (T.S. Lumpe).

produce reliable structures and parts. Computational design tools, such as multi-material optimization algorithms, are employed to leverage that design freedom. In particular, different materials are spatially distributed to increase the functional performance of structures [12,13] or introduce multifunctionality [14]. The rapidly developing field of 4D printing, i.e. 3D printed structures that can actively change their properties under environmental influences, also utilizes the possibility to monolithically print multiple materials [15]. These structures take advantage of differences in the thermomechanical properties of shape memory polymers that can be used to sequentially recover the initial folded state of structures [16], design active shape morphing strips and sheets [17], or to create an autonomous swimming robot [18]. All of these parts and structures are composed of complex material distribution patterns with numerous interfaces among the different materials. To ensure compliance between the designed structures and the final products, extensive knowledge about the exact interfacial behavior between the materials is, therefore, essential.

Numerous studies exist that characterize the influence of process parameters on mechanical [19–22] and thermo-mechanical [23–26] properties, and on the geometric accuracy [27–30] in material jetting. However, little is known about the behavior of interfaces between different materials [31]. This is particularly important in AM, where the process and process parameters can significantly affect the material properties, which is not necessarily the case in conventional fabrication processes. This study, therefore, focuses on the mechanical characterization of the interface strength between different materials in structures printed with the material jetting technology.

2. Background

In the material jetting process, a liquid base material is jetted by a heated print head onto a substrate and typically cured thermally or through UV light. This procedure is repeated for each layer until the final height of the part is reached [8]. The most common commercially available multi-material jetting process is the PolyJet process (Stratasys Ltd.) [32]. In this process, the jetting nozzles in the print head are able to switch between multiple materials, including support material for overhanging features. Fig. 1 shows schematically the print tray and the respective print head movement. Material is extruded and cured with UV light while the print head moves in the x-direction. Rollers smooth out

the deposited material and prepare the surface for the next layer. After moving back and forth at the same y-coordinate, the print head moves in the y-direction and prints the next portion of the current layer until the layer is finished. To print the next layer, the print tray moves down the height of one layer, before the same procedure repeats [33].

This process introduces strong anisotropy in the printed parts, caused by interfaces between nozzles, print head movements, and layers [20,27,34–36]. It is found that quasi-static material properties, such as the ultimate strength and Young's modulus, for a commonly used rigid material (VeroWhitePlus, Stratasys Ltd.) do not vary significantly between printing directions of x- and y-, but are significantly reduced in the z-direction. Material properties in directions between the printer's main axes show that the weakest direction is between 45° and 60° with respect to all three axes, possibly due to shear planes [36].

Other studies investigate the influence of the printing process parameters on the material properties. Mueller et al. [33] analyze, among others, the position on the print table, the storage time between printing and testing, and the storage conditions. They conclude that almost all investigated factors have a statistically significant effect on the final material properties. This includes a strong time dependency of the material properties, in particular in the first 24 h after printing. Thus, in order to create reproducible results, all these parameters should be kept constant when comparing different parts or batches.

Moore and Williams [37,38] investigate the tensile fatigue interface behavior under cyclic loading. Combinations of materials are tested at different pre-strains and up to 1,000,000 cycles. On average, specimens with a multi-material interface do not show a reduced fatigue life compared to the base materials themselves, but erratic failure happens more often. Specimens printed with a “glossy” print option, which means that all surfaces that are not covered in support material exhibit a shiny surface, exhibit an increased interface strength. It is assumed that voids, inherent to the printing process and more prominent at multi-material interfaces, cause the premature failure. Kaweesa et al. [39] compare the fatigue behavior of interfaces with a gradient, i.e. the two constituent materials are blended on a voxel level, and interfaces without a gradient, i.e. both materials are printed right next to each other. It is found that gradients are often weaker than the direct connection and thus should be avoided. Mueller et al. [40] extend the examination of interfaces to the micro-scale. They investigate interfaces between two base materials (VeroWhitePlus and TangoBlackPlus, Stratasys Ltd.) and

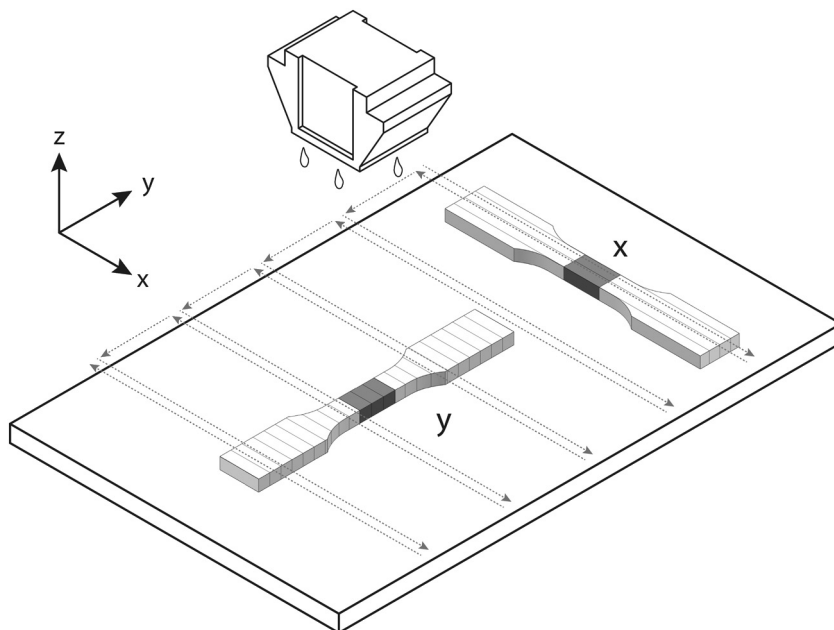


Fig. 1. Schematic of the print tray, the print head and the two main print orientations of the 3D printed specimens' longitudinal axes (x- and y-direction). Dashed arrows indicate the path of the print head while printing one layer. The lines on the specimens schematically show the effect of the printing direction on the material orientation in the parts.

mixes of these materials in different ratios. The mixing process is found to be not a continuous mixing of the base-polymers, but rather a composite embedding where one base material serves as a matrix with inclusions of the second base material. This introduces a local anisotropy at the micro-level. Further investigations on multi-material interfaces include the analytical work of Kumar et al. [41] on single-lap joints. They conclude that the stresses can be significantly reduced by geometric gradients, i.e. tapering the adherents. The strength of the joint on the material-level is not considered. Vu et al. [42,43] also investigate the adhesive behavior between layers of different materials. It is found that failure mostly occurs at the interfaces between layers and parameters like the printing direction, post curing, and strain rate have an influence on the fracture resistance of the specimens. However, a systematic investigation of the interface strength for quasi-static loading is not found in literature.

3. Methods

3.1. Materials and fabrication of samples

All test specimens are printed on a Stratasys Connex3 Objet500 3D printer (Stratasys Ltd., Eden Prairie, MN, USA) using the PolyJet material jetting technology [44]. The printer can mix two base materials to form twelve additional digital materials, which are predefined by the manufacturer. All specimens are printed in the digital material mode, which is required if multiple materials are printed simultaneously [45]. To keep

the printing and testing conditions constant, specimens are prepared according to the findings in Mueller et al. [33]:

- Specimens are positioned evenly spaced and close to the origin in the x-/y-plane of the printing table.
- Base materials from the same batches of identical expiry date are used.
- The printing nozzles are cleaned with isopropanol before each print.
- The specimens are printed with the “matte” print option, i.e. they are fully covered in support material.
- The support material is removed mechanically right after printing, i.e. no water-jet or chemicals are used.
- The specimens are stored in a dark place that is air-conditioned to room temperature ($T = 23\text{ }^{\circ}\text{C}$).
- The specimens are tested approximately 24 h after printing.

For this study, VeroWhitePlus (VW) and TangoBlackPlus (TB) are chosen as base materials, as they possess significantly different mechanical properties at room temperature. VW is rigid at room temperature and formed from isobornyl acrylate, acrylic monomer, urethane acrylate, epoxy acrylate, acrylic monomer, acrylic oligomer and a photoinitiator. TB is rubbery at room temperature and built from urethaneacrylate oligomer, Exo-1,7,7-trimethylbicyclo hept-2-yl acrylate, methacrylate oligomer, polyurethane resin and photoinitiator [46,47]. Fig. 2a shows an overview of the available two base materials and possible combinations of them. For simplification, the material

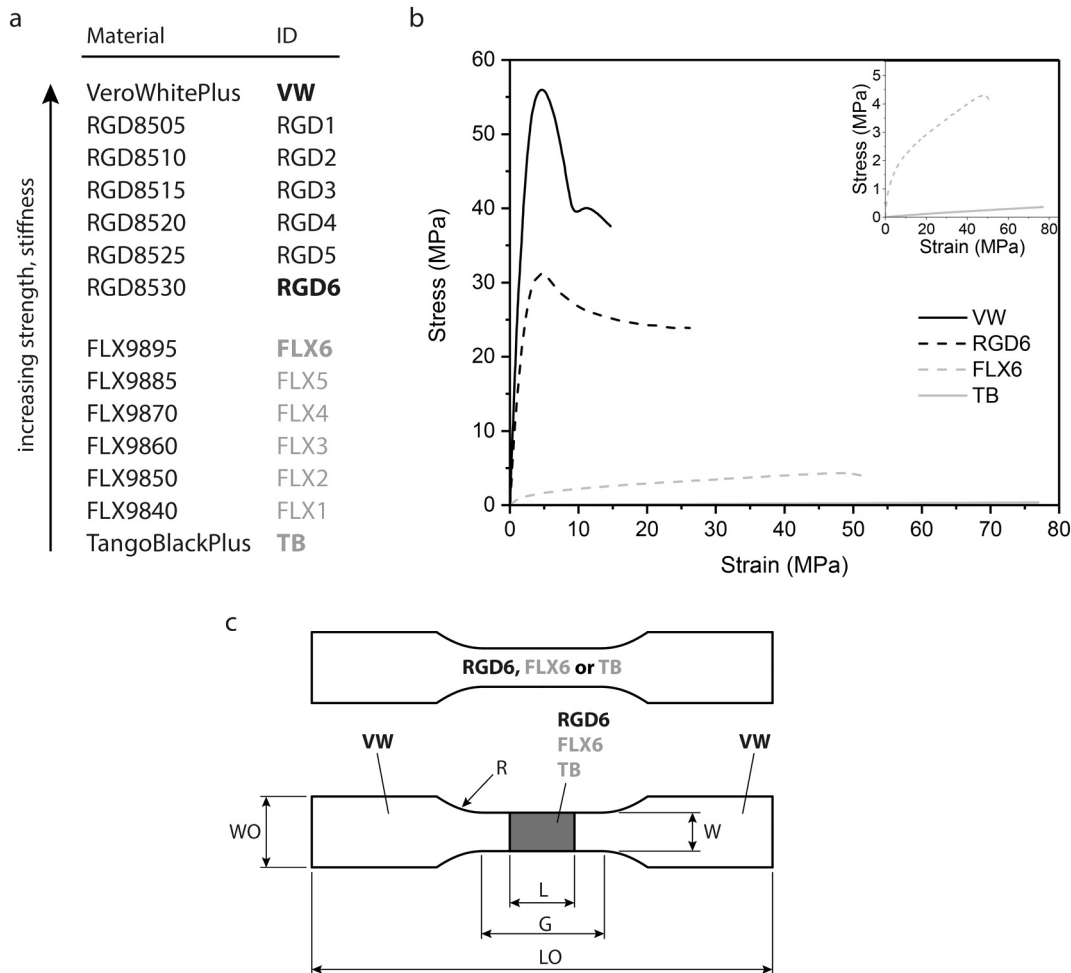


Fig. 2. (a) Overview of the two base materials VeroWhitePlus (VW) and TangoBlackPlus (TB), the different digital materials printable from these two base materials with the Stratasys Connex3 Objet500, and the IDs as used in this study. (b) Stress-strain-curves of the four materials used in this work. (c) Top: single-material specimens consist of only one material, i.e. RGD6, FLX6 or TB. Bottom: adapted specimen geometry with one material (VW) in the outer gripping areas and a second material (RGD6, FLX6 or TB) in the middle.

names as provided by the manufacturer (Fig. 2a, left column) are replaced by IDs (Fig. 2a, right column). Fig. 2b shows the qualitative stress-strain responses for VW, RGD6, FLX6 and TB, where RGD6 and FLX6 are two digital materials. The other digital materials are omitted in this plot as the stress-strain curves are similar to the ones shown and lie in between the curves of VW/RGD6 and TB/FLX6 respectively [48]. Two groups of materials are identified: (i) rigid materials based on VW (VW, RGD1–6) that have a high Young's modulus and ultimate tensile strength (UTS), but a low failure strain; (ii) flexible materials based on TB (TB, FLX1–6) that have a lower Young's modulus and UTS, but a high failure strain. Based on the similar material behavior within these groups and assuming that multi-material structures fail either in the weakest material or at the interface, the following material combinations are investigated in this work: VW and RGD6, VW and FLX6, and VW and TB.

As the print direction has a large effect on the material properties, we assume that the same holds for the interface behavior. Thus, dogbone specimens are printed with the longitudinal axis parallel to the x - and y -direction of the printer. This is also the direction of the normal of the respective interface between two different materials, i.e. the plane between white and gray material as schematically shown in Fig. 1. In this study, the two printing directions and thus the directions of the interfaces are referred to as interfaces in the x - and y -direction respectively. To ensure statistical significance of the obtained results, 30 specimens are printed and tested for each material combination and printing direction. Invalid specimens, e.g. specimens that slip during testing, are removed from the dataset. This leaves a minimum of 25 specimens for each combination. Further, 30 specimens of RGD6, FLX6 and TB for both printing directions are printed and tested as a reference accordingly.

3.2. Testing procedure

Tensile tests are conducted according to the ASTM D638-14 standard [49] to determine the stress-strain curve and the UTS (σ_u) of the specimens. Two types of specimens are tested: (i) single-material specimens from RGD6, FLX6, and TB (Fig. 2c, top) and (ii) multi-material specimens with VW in the outer gripping areas and a second material (RGD6, FLX6 or TB) in the gauge area (Fig. 2c, bottom). As no standard exists for testing the interface behavior in multi-material structures [31], the specimen geometries suggested in the ASTM norm are adapted as follows. The second material is inserted in the gauge symmetrically with an overall length L of 10.0 mm. The gauge length, G , is extended to 18 mm to obtain a region with constant stress over the whole cross-section to minimize boundary effects from the radius, R , of 12.7 mm, for both materials. The gauge width, W , is increased to 6.0 mm to achieve a plane stress state and the overall width, W_0 , is increased to 11.0 mm. The thickness, T , of 3.2 mm is adopted from the standard.

Both multi-material and single-material specimen types are printed with the same outside dimensions. Fig. 2c shows the final specimen geometry with all relevant parameters.

An Instron ElectroPuls E3000 testing machine with a Dynacell load cell of 5kN capacity is used in combination with an AVE 2 (advanced video extensometer) non-contacting video extensometer to record the deformation in the narrow section. Dots on the specimens, applied with a commercially available permanent marker, are used as a reference. For the single-material specimens, the distance between the dots represents the gauge length, G . For the multi-material specimens, the dots are positioned on the inner material about 1 mm away from the interface. The stress is obtained by dividing the measured load by the original undeformed cross-sectional area of the specimen. The strain is obtained by dividing the elongation of the narrow section as measured with the video extensometer by its original undeformed length.

As the material properties of polymers are typically strain-rate dependent, the actual strain rate within the specimens is taken into account. Due to different stiffnesses of the materials, the strain rate differs between different specimen types, i.e. the different materials and single-/multi-material specimen types. The strain is inversely proportional to the cross-sectional area and Young's modulus of the specimen. The cross-sectional area in the gauge area is the same for all specimens, but the Young's modulus varies for the multi-material specimens between the outer and inner region. Thus, for a given overall deformation, i.e. separation of the testing machine grippers, the strain in the inner part of a multi-material specimen can be significantly higher than in the respective single-material specimen. This is particularly true in multi-material specimens with a compliant inner material, like TB, where mostly this compliant phase is deformed. To account for this, both single material and multi-material specimens are tested over a range of strain rates. Testing speeds are chosen such that strain rates between $\dot{\epsilon} \approx 0.06\%/s$ and $\dot{\epsilon} \approx 1.9\%/s$ are achieved. This results in testing speeds between 1 mm/min and 25 mm/min for single material specimens, and 1 mm/min and 17 mm/min for multi-material specimens. The UTS of all specimens is evaluated after testing. In literature, a logarithmic relation between the UTS and the strain rate of the following form is suggested [50]:

$$\sigma_y = \sigma_0 + \sigma_1 \log(\dot{\epsilon}_p / \dot{\epsilon}_0), \quad (1)$$

where σ_y is the UTS at the strain rate $\dot{\epsilon}_p$, σ_0 is the UTS at the strain rate $\dot{\epsilon}_0$ and σ_1 is a material-dependent constant. The results from the single-material tests are fit according to Eq. (1). The results from the multi-material tests are then compared to the results from the single-material tests. Further, it is recorded if the multi-material specimens fail at the interface or in the softer material.

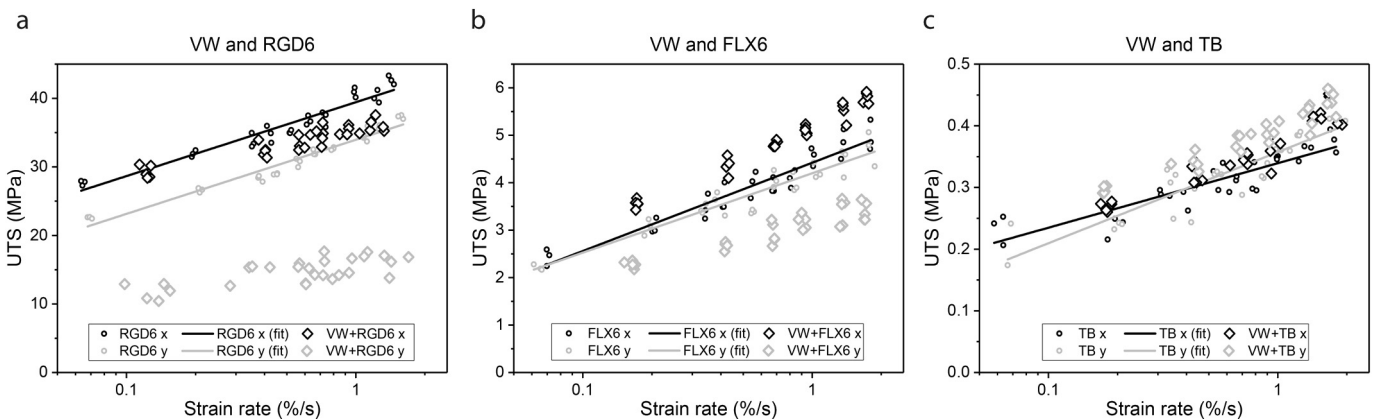


Fig. 3. Ultimate tensile strength (UTS) at different strain rates in the x - and y -direction (black and gray). Circle markers show the UTS of the single-material specimens of pure RGD6 (a), FLX6 (b) and TB (c) at different strain rates. Solid lines show the fit curves according to Eq. (1) respectively. The diamond markers represent the UTS of the tested multi-material specimens with VW outside and the inner part RGD6 (a), FLX6 (b) and TB (c), respectively.

Table 1
Parameters for Eq. (1) that describe the relation between UTS and strain rate for pure RGD6, FLX6 and TB in both x- and y-direction.

		σ_0	σ_1	ε_0	R-square
RGD6	x	-19.47	10.78	<0.01	0.92
	y	-19.26	10.82	<0.01	0.95
FLX6	x	1.76	1.86	0.04	0.91
	y	1.79	1.67	0.04	0.90
TB	x	0.47	0.10	16.96	0.79
	y	0.50	0.15	9.01	0.82

4. Results

Fig. 3 shows the ultimate tensile strength of specimens printed in the x-direction (black) and y-direction (gray). The circle markers show the test values of all single-material specimens, i.e. pure RGD6 (Fig. 3a), FLX6 (Fig. 3b), and TB (Fig. 3c). The solid lines represent the fit curves according to Eq. (1) for each material data set respectively. The fitting parameters are provided in Table 1. For the rigid VW based material RGD6, the x-direction is considerably stronger than the y-direction

(Fig. 3a). The fit relation for RGD6 x (black) is similar to that for RGD6 y (gray), but shifted upwards by about 5 MPa thus exhibiting a higher UTS. However, for the flexible TB based materials (FLX6 and TB), the printing direction has little effect on the strength as the fit relations for both directions in both cases are almost identical (Fig. 3b and c).

The diamond markers in Fig. 3 represent the results from the multi-material tests with VW + RGD6 (Fig. 3a), VW + FLX6 (Fig. 3b), and VW + TB (Fig. 3c) in the x-direction and y-direction, respectively. For VW + RGD6 (Fig. 3a), the difference in strength between the x-direction and y-direction is even larger. The strength of the VW + RGD6 specimens in the x-direction (black diamond markers) almost reaches that of the pure RGD6 specimens (black line), but is significantly lower in the y-direction (gray diamond markers and line). For the material combination VW + FLX6 (Fig. 3b), the multi-material specimens in the x-direction are stronger than pure FLX6, whereas specimens in the y-direction exhibit weaker properties when compared to the pure FLX6 material. Fig. 3c shows little difference between the different print orientations for VW + TB multi-material specimens, which both are slightly stronger than the pure TB single-material specimens.

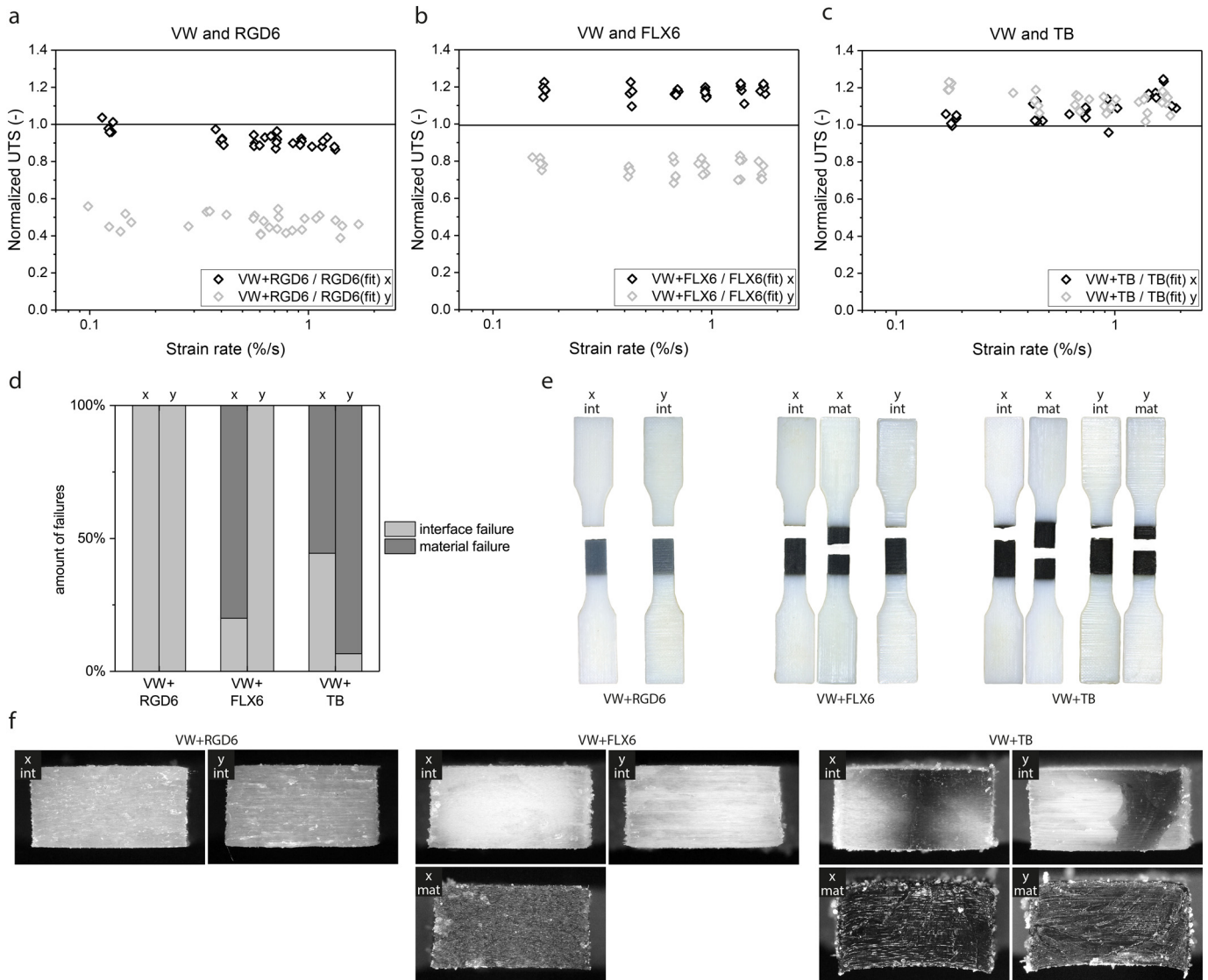


Fig. 4. (a)–(c) UTS of the multi-material specimens VW/RGD6 (a), VW/FLX6 (b), and VW/TB (c) divided by the UTS of the respective single-material specimens RGD6 (a), FLX6 (b), TB (c). (d) Percentage of failures of the multi-material specimens at the interface (light gray) and in the weaker material (dark gray) for the three material combinations in both print directions. (e) Multi-material specimens of each material combination, print direction (x or y) and failure location (interface or material). (f) Microscope images of fracture surfaces of the specimens from (e). All images show the surface of the upper parts of the fractured specimens.

Fig. 4a–c show the UTS from the multi-material specimens VW + RGD6, VW + FLX6, and VW + TB normalized with the UTS for pure RGD6, FLX6, and TB, extracted from the fit curves, respectively. In Fig. 4a, it can be seen that the VW + RGD6 specimens printed in y-direction are 50% weaker than pure RGD6 (solid line) and specimens printed in the x-direction. A similar difference between the x-direction and y-direction is observed for VW + FLX6 (Fig. 4b). In the y-direction, the VW + FLX6 specimens are 20% weaker than pure FLX6 and in the x-direction 20% stronger. For VW + TB (Fig. 4c), the tensile strengths in the x- and y-direction are almost identical and, on average, 10% stronger than pure TB.

Fig. 4d shows the percentage of failures at the interface and in the weaker, inner material for the multi-material specimens. As for all three material combinations the material on the inside of the specimens is weaker than that on the outside, failure is either possible in the region of the weaker material or at the interface between the two materials. All VW + RGD6 specimens fail at the interface, independent of the print direction. For the combination of VW + FLX6, all specimens printed in the y-direction fail at the interface, whereas 80% of the specimens printed in x-direction fail inside the FLX6-material. In the group of VW + TB, 45% of the x-direction specimens fail at the interface, whereas 93% of those printed in y-direction fail in the TB material. In cases where both failure types occur, no statistically significant difference between the UTS of specimens that fail at the interface and the UTS of specimens that fail in the material is found. Interface and material failures are evenly distributed over the strain rate range, no failure type occurs significantly more often at specific strain rates. Fig. 4e shows images of one specimen for each tested material combination, printing direction (x or y) and failure location (interface or material) respectively. The fracture surface of the upper part of each fractured specimen is shown in Fig. 4f. The specimens in the first row, which fail at the interface, exhibit a clean VW surface for the combination VW + RGD6, whereas the surfaces of the VW + FLX6 and VW + TB specimens show VW with dark regions or regions of TB still connected to it. On all interface failure surfaces in the y-direction, horizontal lines can be observed. Interface failure surfaces in the x-direction do not show a distinct pattern.

5. Discussion

5.1. Single-material tests

As seen in literature, the material strength for the pure base materials VW and TB is similar for both the x and y printing directions [33].

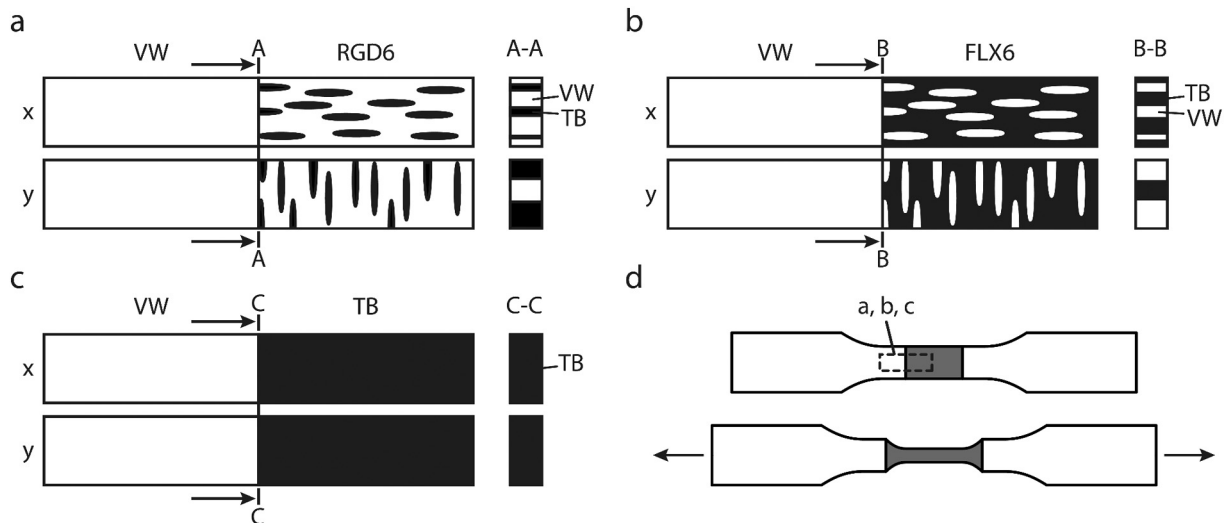


Fig. 5. Schematic of the multi-material interfaces between VW and RGD6 (a), VW and FLX6 (b), VW and TB (c) in both printing directions x (upper) and y (lower) respectively. The digital materials RGD6 and FLX6 are heterogeneous composites on the micro-level with a rigid VW-matrix and elliptical compliant TB inclusions (a) and a compliant TB-matrix and rigid VW inclusions vice versa (b). (d) Necking of the compliant inner material in a multi-material specimen under tensile load compared to the original undeformed specimen geometry.

However, the digital materials show different behavior, i.e., a higher UTS in the x-direction than in the y-direction, which is especially true for pure RGD6, where the specimens oriented in the x-direction are stronger than those in the y-direction. This behavior can be explained by looking at the microstructure of the materials. Mueller et al. [40] showed that the mixing of two base materials results in a composition similar to conventional composite materials. One material is embedded as a second phase in the matrix of the other material and forms elliptical, fiber-like inclusions oriented along the x-axis, parallel to the printing direction. It is known for such composites that the strength along the fiber orientation is significantly higher than perpendicular to the fiber orientation [51–53].

Fig. 5a–c show schematics of the three tested material combinations VW + RGD6, VW + FLX6, and VW + TB for both print directions x (top) and y (bottom). VW as a base material has no inclusions, whereas RGD6, as the most compliant of the possible VW-based digital materials, has a significant number of TB inclusions (Fig. 5a). For pure RGD6, the orientation of the soft inclusions in the strong VW matrix depends on the print orientation. Accordingly, the average cross-section in the x-direction is likely to have many small inclusions, whereas in the y-direction, the average cross-section has fewer and larger inclusions. While the average amount of soft material over all cross-sections is approximately the same in the x-direction and the y-direction, the variations are larger in the y-direction, i.e. some cross-sections are much stronger compared to the specimens printed in the x-direction and some are much weaker. Since the weakest cross-section determines the overall strength, the RGD6 specimens printed along the y-direction tend to be weaker than those printed in the x-direction.

For the opposite composition of a compliant TB matrix with rigid VW inclusions (FLX6 material in Fig. 5b), the strengthening of the inclusions seems to be dominant, which is similar to classic composite structures [53]. Similar to composite structures reinforced with short fibers, the inclusions are local inclusions rather than continuous fibers. Thus, the effect of the orientation of the inclusions is smaller compared to composites reinforced with continuous long fibers [54], causing a similar strength in the x-direction and the y-direction (Fig. 4b). As there are no inclusions in pure TB, similar behavior of the UTS in the x-direction and the y-direction is observed (Fig. 4c).

5.2. Multi-material tests

The microstructure of the materials also determines the interfacial strength in multi-material specimens. In the case of VW + RGD6 (Fig. 5a), the VW base material is connected to RGD6, which is a

combination of VW matrix material and softer TB inclusions. Under loading, the cross-section of the softer RGD6 material is reduced (Fig. 5d) and a kink occurs near the interface, which locally induces stresses (bottom image). Thus, the specimens fail at slightly lower external loads than the respective pure RGD6 specimens (Fig. 4a). Specimens printed in the y-direction are already weaker due to the larger inclusions, as shown in the previous section. The induced stress further reduces the specimens' strength and triggers failure at lower UTS compared to the x-direction.

Fig. 5b shows the combination VW + FLX6, where pure VW is connected to a soft TB matrix with VW inclusions. In this example, the VW inclusions increase the effective surface area of the interface, strengthening the interface. Due to the orientation of the inclusions, the increase in surface area of the interface is large in the x-direction, as seen in Fig. 5b, and the resulting increase in strength larger than the reduction in strength due to necking and associated stress concentrations (Fig. 4b). In the y-direction, the contact surface is only slightly increased. Higher stress concentrations at the interface due to necking are expected, which leads, again, to failure at the interface at lower stresses. Due to this weaker interface, all VW + FLX6 specimens in the y-direction tend to fail at the interface, whereas in the x-direction failure occurs both at the interface and in the softer FLX6 material. It seems that the material and the interface exhibit an equally increased strength for this material combination and printing direction.

As there are no inclusions in either material of the VW + TB combination, little difference is seen between the interface and material strength in the x-direction and the y-direction in terms of the UTS of the specimens (Fig. 4c). This indicates that the interfaces between the two pure base materials are stronger than the TB material, as they withstand increased stresses due to strong necking without suffering from premature failure. Similarly to VW + FLX6, the specimens that fail in the softer material and not at the interface show a slightly higher UTS than pure TB itself, hinting that the same strengthening effects in these multi-material parts occur.

Besides these microstructural effects, it is prevalent in additive manufacturing generally and particularly in material jetting that the process has a significant effect on the overall mechanical properties of printed parts [33]. Smearing between phases of different connected materials is common due to mechanical flattening of the surface using rollers mounted on the print head after each deposited layer. In particular, in digital materials and structures with small features of different materials, the interfaces are continuous on a micrometer level, rather than completely separated [40]. Mechanical properties of both constituent materials can be affected by this smearing and mixing at the interface, which might also contribute to the increased strength of some of the multi-material specimens. The fracture surfaces in Fig. 4f partly reflect this: no mixing and, thus, no additional strengthening occurs at the VW + RGD6 interfaces. Darker areas at the VW + FLX6 interfaces and large areas of TB at the VW + TB interfaces imply that smearing is happening for these material combinations, strengthening the weaker material.

These smearing effects together with the micromechanics of the matrix/inclusion interactions seem to be the main factors determining the interface strength in parts printed with material jetting. As they originate from the printing process itself, it is assumed that our findings are applicable to all material jetting processes with a similar thermomechanical process, i.e. the jetting of multiple materials simultaneously, print head movement, UV curing, and the flattening of a layer using rollers. Due to the consistent mechanical behavior of the investigated materials within both groups (VW-based and TB-based, Fig. 2), the combinations investigated in this study represent boundaries for the expected interface behavior of these materials. Hence, the results can be directly applied to other material combinations from the VW-TB range.

In summary, the trends identified in this work can be generalized for interface and material strength in multi-material structures printed with the material jetting process:

- (1) In the majority of cases, interfaces in the x-direction are at least as strong as the weaker of the connected materials, i.e. the interface does not add a weak spot.
- (2) The interfacial strength of specimens printed in the y-direction depends on the material combinations. If both of the connected materials are pure base materials, the interface is at least as strong as the weaker of the connected materials. If either of the materials is a digital material, the interfacial strength is reduced.
- (3) Specimens with two rigid (VW based) materials fail at the interface, regardless of the base or digital materials. As seen in (1) and (2), this does not necessarily affect the effective strength.

The design of multi-material parts is, therefore, not trivial and the process parameters need to be taken into account. In addition to findings from previous research [33], the combination of materials needs to be considered as well as the orientation of interfaces between adjacent materials. Hence, the following guidelines are derived for designing multi-material structures manufactured via material jetting.

In the majority of the cases, interfaces in the x-direction do not require separate treatment, as they are not weaker than the weaker of the connected materials. An increase in the interfacial strength of up to 20% can be assumed for combinations of VW and TB based materials (VW + FLX6, VW + TB) in this direction. Multi-material interfaces in the y-direction exhibit a reduction in strength of up to 50% and should be avoided. Interfaces between pure VW and pure TB do not have to be treated separately, as they are never weaker than pure TB itself. An increase in strength of up to 10% can be expected. Thus, by designing parts to avoid “weak” interface directions, materials at the extremes of the spectrum in rigidity can be printed right next to each other without reducing the strength of structures. This behavior has to be considered when designing multi-material parts and structures at the macro-level, but can be also relevant for multi-material features at the microscale as they occur e.g. in voxel-based, functionally graded designs [55]. Interfaces between voxels in the y-direction might introduce weak spots and give rise to crack initiation in the voxelized material, which leads to premature failure of the structure. Avoiding plane interfaces in one direction by using e.g. polyhedron “voxels” might help to prevent this.

6. Conclusions

Recent advances in additive manufacturing technology enable the fabrication of monolithic, multi-material parts and structures. The findings in this work present an important step towards the understanding of the microstructural mechanics and properties of such 3D printed parts, focusing on the interfacial behavior. Applying systematic specimen manufacturing and testing methods, the tensile strength of these interfaces for selected material combinations at different strain rates is investigated. We show that the strength of interfaces in inkjet 3D printed multi-material parts is dependent on both geometric parameters, i.e. the orientation of the interfaces with respect to the printing directions, and on the connected materials themselves. Structures designed using the results presented here can benefit from up to 20% increased strength and avoid failure at 50% reduced strength. As the results obtained in this study are investigated on a microstructural level, they are independent of the specific process and generally applicable to material jetting processes. While this knowledge allows for predicting and simulating structural properties more accurately, it also enables the design of more efficient structures through, for example, optimization algorithms. This is particularly interesting in areas that are limited in space and weight, or in areas requiring high performance, such as automotive, aerospace and sports equipment.

CRedit authorship contribution statement

Thomas S. Lumpe: Formal analysis, Writing - original draft, Writing - review & editing, Conceptualization, Investigation. **Jochen Mueller:** Formal

analysis, Writing - original draft, Writing - review & editing, Conceptualization. **Kristina Shea:** Supervision, Writing - original draft, Writing - review & editing, Conceptualization.

Acknowledgements

The authors acknowledge David Kovacs for his help with the material testing.

The raw and processed data required to reproduce these findings cannot be shared at this time due to technical or time limitations. Data is available upon request.

Data statement

The raw and processed data required to reproduce these findings cannot be shared at this time due to technical or time limitations. Data is available upon request.

Declarations of interest

None.

Author contributions

T.S.L., J.M. and K.S. conceived the study. T.S.L. and J.M. designed the experiments. T.S.L. conducted the experimental work. T.S.L. and J.M. analyzed the results. T.S.L., J.M. and K.S. wrote and reviewed the manuscript.

References

- [1] A. Bandyopadhyay, B. Heer, Additive manufacturing of multi-material structures, *Mater. Sci. Eng. R. Rep.* 129 (2018) 1–16, <https://doi.org/10.1016/j.msere.2018.04.001>.
- [2] B.J. De Gans, P.C. Duineveld, U.S. Schubert, Inkjet printing of polymers: state of the art and future developments, *Adv. Mater.* 16 (2004) 203–213, <https://doi.org/10.1002/adma.200300385>.
- [3] E.A. Clark, M.R. Alexander, D.J. Irvine, C.J. Roberts, M.J. Wallace, S. Sharpe, J. Yoo, R.J.M. Hague, C.J. Tuck, R.D. Wildman, 3D printing of tablets using inkjet with UV photoinitiation, *Int. J. Pharm.* 529 (2017) 523–530, <https://doi.org/10.1016/j.ijpharm.2017.06.085>.
- [4] P.F. Egan, K. Shea, I. Bauer, S.J. Ferguson, Integrative design, build, test approach for biomedical devices with lattice structures, Proceedings of the ASME 2018 International Design Engineering Technical Conferences and Computers and Information in Engineering Conference (IDETC/CIE 2018), Quebec City, Canada 2018, pp. 1–9.
- [5] J. Lessing, A.C. Glavan, S.B. Walker, C. Keplinger, J.A. Lewis, G.M. Whitesides, Inkjet printing of conductive inks with high lateral resolution on omniphobic “rF paper” for paper-based electronics and MEMS, *Adv. Mater.* 26 (2014) 4677–4682, <https://doi.org/10.1002/adma.201401053>.
- [6] G. Hu, T. Albrow-Owen, X. Jin, A. Ali, Y. Hu, R.C.T. Howe, K. Shehzad, Z. Yang, X. Zhu, R.I. Woodward, T.C. Wu, H. Jussila, J. Bin Wu, P. Peng, P.H. Tan, Z. Sun, E.J.R. Kelleher, M. Zhang, Y. Xu, T. Hasan, Black phosphorus ink formulation for inkjet printing of optoelectronics and photonics, *Nat. Commun.* 8 (2017) <https://doi.org/10.1038/s41467-017-00358-1>.
- [7] M. Gao, L. Li, Y. Song, Inkjet printing wearable electronic devices, *J. Mater. Chem. C* 5 (2017) 2971–2993, <https://doi.org/10.1039/c7tc00038c>.
- [8] P. Calvert, Inkjet printing for materials and devices, *Chem. Mater.* 13 (2001) 3299–3305, <https://doi.org/10.1021/cm0101632>.
- [9] Y. Zhang, F. Zhang, Z. Yan, Q. Ma, X. Li, Y. Huang, J.A. Rogers, Printing, folding and assembly methods for forming 3D mesostructures in advanced materials, *Nat. Rev. Mater.* 2 (2017) <https://doi.org/10.1038/natrevmats.2017.19>.
- [10] E. Saleh, P. Woolliams, B. Clarke, A. Gregory, S. Greedy, C. Smart, R. Wildman, I. Ashcroft, R. Hague, P. Dickens, C. Tuck, 3D inkjet-printed UV-curable inks for multi-functional electromagnetic applications, *Addit. Manuf.* 13 (2017) 143–148, <https://doi.org/10.1016/j.addma.2016.10.002>.
- [11] Stratasys, PolyJet materials data sheet, http://global72.stratasys.com/~media/Main/Files/Material_Spec_Sheets/MSS_PJ_PJMaterialsDataSheet_0517aWeb.pdf?la=de 2018, Accessed date: 21 January 2018.
- [12] Y. Hu, G.M. Fadel, V.Y. Blouin, D.R. White, Optimal design for additive manufacturing of heterogeneous objects using ultrasonic consolidation, *Virtual Phys. Prototyp.* 1 (2006) 53–62, <https://doi.org/10.1080/17452750500271355>.
- [13] T. Stankovic, J. Mueller, P. Egan, K. Shea, A. Generalized Optimality, Criteria method for optimization of additively manufactured multimaterial lattice structures, *J. Mech. Des.* 137 (2015) 1–12, <https://doi.org/10.1115/1.4030995>.
- [14] Y. Wang, J. Gao, Z. Luo, T. Brown, N. Zhang, Level-set topology optimization for multimaterial and multifunctional mechanical metamaterials, *Eng. Optim.* 0273 (2016) 1–21, <https://doi.org/10.1080/0305215X.2016.1164853>.
- [15] A.S. Gladman, E.A. Matsumoto, R.G. Nuzzo, L. Mahadevan, J.A. Lewis, Biomimetic 4D printing, *Nat. Mater.* 15 (2016) 413–418, <https://doi.org/10.1038/nmat4544>.
- [16] Y. Mao, K. Yu, M.S. Isakov, J. Wu, M.L. Dunn, H. Jerry Qi, Sequential self-folding structures by 3D printed digital shape memory polymers, *Sci. Rep.* 5 (2015) <https://doi.org/10.1038/srep13616>.
- [17] Z. Ding, C. Yuan, X. Peng, T. Wang, H.J. Qi, M.L. Dunn, Direct 4D printing via active composite materials, *Sci. Adv.* 3 (2017), e1602890, <https://doi.org/10.1126/sciadv.1602890>.
- [18] T. Chen, O.R. Bilal, K. Shea, C. Daraio, Harnessing bistability for directional propulsion of untethered, soft robots, *Proc. Natl. Acad. Sci.* (2018) <https://doi.org/10.1073/pnas.1800386115>.
- [19] A. Cazón, P. Morer, L. Matey, PolyJet technology for product prototyping: tensile strength and surface roughness properties, *Proc. Inst. Mech. Eng. B J. Eng. Manuf.* 228 (2014) 1664–1675, <https://doi.org/10.1177/0954405413518515>.
- [20] A. Keşy, J. Kotliński, Mechanical properties of parts produced by using polymer jetting technology, *Arch. Civ. Mech. Eng.* 10 (2010) 37–50, [https://doi.org/10.1016/S1644-9665\(12\)60135-6](https://doi.org/10.1016/S1644-9665(12)60135-6).
- [21] J.E. Ryu, E. Salcedo, H.J. Lee, S.J. Jang, E.Y. Jang, H. Al Yassi, D. Baek, D. Choi, E. Lee, Material models and finite analysis of additively printed polymer composites, *J. Compos. Mater.* (2018) <https://doi.org/10.1177/0021998318785672>.
- [22] E. Salcedo, D. Baek, A. Berndt, J.E. Ryu, Simulation and validation of three dimension functionally graded materials by material jetting, *Addit. Manuf.* 22 (2018) 351–359, <https://doi.org/10.1016/j.addma.2018.05.027>.
- [23] D. Blanco, P. Fernandez, A. Noriega, Nonisotropic experimental characterization of the relaxation modulus for PolyJet manufactured parts, *J. Mater. Res.* 29 (2014) 1876–1882, <https://doi.org/10.1557/jmr.2014.200>.
- [24] K.K. Reichl, D.J. Inman, Dynamic modulus properties of objet Connex 3D printer digital materials, Topics in Modal Analysis & Testing, Springer International Publishing 2016, pp. 191–198, <https://doi.org/10.1007/978-3-319-30249-2>.
- [25] K.K. Reichl, D.J. Inman, Dynamic mechanical and thermal analyses of objet Connex 3D printed materials, *Exp. Tech.* 42 (2018) 19–25, <https://doi.org/10.1007/s40799-017-0223-0>.
- [26] S. Akbari, A.H. Sakhaei, K. Kowsari, B. Yang, A. Serjouei, Z. Yuanfang, Q. Ge, Enhanced multimaterial 4D printing with active hinges, *Smart Mater. Struct.* 27 (2018) <https://doi.org/10.1088/1361-665X/aab663>.
- [27] M.W. Barclift, C.B. Williams, Examining variability in the mechanical properties of parts manufactured by PolyJet direct 3D printing, International Solid Freeform Fabrication Symposium 2012, pp. 876–890.
- [28] S.Y. Hong, Y.C. Kim, M. Wang, H.I. Kim, D.Y. Byun, J. Do Nam, T.W. Chou, P.M. Ajayan, L. Ci, J. Suhr, Experimental investigation of mechanical properties of UV-Curable 3D printing materials, *Polymer* 145 (2018) 88–94, <https://doi.org/10.1016/j.polymer.2018.04.067>.
- [29] Y.L. Yap, C. Wang, S.L. Sing, V. Dikshit, W.Y. Yeong, J. Wei, Material jetting additive manufacturing: an experimental study using designed metrological benchmarks, *Precis. Eng.* (2017) <https://doi.org/10.1016/j.precisioneng.2017.05.015>.
- [30] A. Khoshkhou, A.L. Carrano, D.M. Bliersch, Effect of surface slope and build orientation on surface finish and dimensional accuracy in material jetting processes, *Procedia Manuf.* 26 (2018) 720–730, <https://doi.org/10.1016/j.promfg.2018.07.082>.
- [31] J.R.C. Dizon, A.H. Espera, Q. Chen, R.C. Advincula, Mechanical characterization of 3D-printed polymers, *Addit. Manuf.* 20 (2018) 44–67, <https://doi.org/10.1016/j.addma.2017.12.002>.
- [32] Stratasys, PolyJet technology, <http://www.stratasys.com/de/polyjet-technology> 2018.
- [33] J. Mueller, K. Shea, C. Daraio, Mechanical properties of parts fabricated with inkjet 3D printing through efficient experimental design, *Mater. Des.* 86 (2015) 902–912, <https://doi.org/10.1016/j.matdes.2015.07.129>.
- [34] L. Bass, N.A. Meisel, C.B. Williams, Exploring variability of orientation and aging effects in material properties of multi-material jetting parts, *Rapid Prototyp. J.* 22 (2016) 826–834, <https://doi.org/10.1108/RPJ-11-2015-0169>.
- [35] P. Gay, D. Blanco, F. Pelayo, A. Noriega, P. Fernández, Analysis of factors influencing the mechanical properties of flat PolyJet manufactured parts, *Procedia Eng.* 132 (2015) 70–77, <https://doi.org/10.1016/j.proeng.2015.12.481>.
- [36] J. Mueller, K. Shea, The effect of build orientation on the mechanical properties in inkjet 3D printing, International Solid Freeform Fabrication Symposium 2015, Austin, Texas 2015, pp. 983–992.
- [37] J.P. Moore, C.B. Williams, Fatigue characterization of 3D printed elastomer material, Solid Freeform Fabrication Symposium 2012, pp. 641–655.
- [38] J.P. Moore, C.B. Williams, Fatigue properties of parts printed by PolyJet material jetting, *Rapid Prototyp. J.* 21 (2015) 675–685, <https://doi.org/10.1108/RPJ-03-2014-0031>.
- [39] D.V. Kaweesa, D.R. Spillane, N.A. Meisel, Investigating the impact of functionally graded materials on fatigue life of material jetted specimens, Proceedings of the 28th Annual International Solid Freeform Fabrication Symposium – An Additive Manufacturing Conference 2017, pp. 578–592.
- [40] J. Mueller, D. Courty, M. Spielhofer, R. Spolenak, K. Shea, Mechanical properties of interfaces in inkjet 3D printed single- and multi-material parts, *3D Print. Addit. Manuf.* 4 (2017) 193–199, <https://doi.org/10.1089/3dp.2017.0038>.
- [41] S. Kumar, M. de Tejada Alvaro, Modeling and experimental evaluation of geometrically graded multi-material single-lap joints, 56th AIAA/ASCE/AHS/ASC Structures, Structural Dynamics, and Materials Conference, AIAA, Kissimmee, Florida 2015, pp. 1–25.
- [42] I. Vu, L. Bass, N. Meisel, B. Orlor, C.B. Williams, D.A. Dillard, Characterization of multi-material interfaces in PolyJet additive manufacturing, Solid Freeform Fabrication Symposium 2014, pp. 959–982, <https://doi.org/10.1007/s13398-014-0173-7.2>.
- [43] I.Q. Vu, L. Bass, C.B. Williams, D.A. Dillard, Characterizing the effect of print orientation on interface integrity of multi-material jetting additive manufacturing, *Addit. Manuf.* 22 (2018) 447–461, <https://doi.org/10.1016/j.addma.2018.05.036>.

- [44] Stratasys, Connex 3 Objet500 and Objet350, <http://www.stratasys.com/3d-printers/objet-350-500-connex3>, Accessed date: 21 January 2018.
- [45] Stratasys, *Objet500 User Guide*, 2018.
- [46] Q. Ge, C.K. Dunn, H.J. Qi, M.L. Dunn, Active origami by 4D printing, *Smart Mater. Struct.* 23 (2014), 094007. <https://doi.org/10.1088/0964-1726/23/9/094007>.
- [47] J.E.M. Teoh, J. An, C.K. Chua, M. Lv, V. Krishnasamy, Y. Liu, Hierarchically self-morphing structure through 4D printing, *Virtual Phys. Prototyp.* 12 (2017) 61–68, <https://doi.org/10.1080/17452759.2016.1272174>.
- [48] T. Chen, J. Mueller, K. Shea, Integrated design and simulation of tunable, multi-state structures fabricated monolithically with multi-material 3D printing, *Sci. Rep.* 7 (2017) 1–8, <https://doi.org/10.1038/srep45671>.
- [49] ASTM International, Standard Test Method for Tensile Properties of Plastics D638–14, 2004 <https://doi.org/10.1520/D0638-14.1>.
- [50] H.F. Brinson, L.C. Brinson, *Polymer Engineering Science and Viscoelasticity*, Second ed. Springer Science & Business Media, New York, 2015 <https://doi.org/10.1007/978-1-4899-7485-3>.
- [51] B.G. Compton, J.A. Lewis, 3D-printing of lightweight cellular composites, *Adv. Mater.* 26 (2014) 5930–5935, <https://doi.org/10.1002/adma.201401804>.
- [52] J.R. Raney, B.G. Compton, J. Mueller, T.J. Ober, K. Shea, J.A. Lewis, Rotational 3D printing of damage-tolerant composites with programmable mechanics, *Proc. Natl. Acad. Sci.* (2018), 201715157. <https://doi.org/10.1073/pnas.1715157115>.
- [53] R.F. Landel, L.E. Nielsen, *Mechanical Properties of Polymers and Composites*, CRC Press, 1993.
- [54] H.R. Lusti, P.J. Hine, A.A. Gusev, Direct numerical predictions for the elastic and thermoelastic properties of short fibre composites, *Compos. Sci. Technol.* 62 (2002) 1927–1934, [https://doi.org/10.1016/S0266-3538\(02\)00106-9](https://doi.org/10.1016/S0266-3538(02)00106-9).
- [55] E.L. Doubrovski, E.Y. Tsai, D. Dikovskiy, J.M.P. Geraedts, H. Herr, N. Oxman, Voxel-based fabrication through material property mapping: a design method for bitmap printing, *Comput. Aided Des.* 60 (2015) 3–13, <https://doi.org/10.1016/j.cad.2014.05.010>.